Acta Pharmaceutica Sinica B 2024;14(2):795−807

Chinese Pharmaceutical Association
Institute of Materia Medica, Chinese Academy of Medical Sciences

Acta Pharmaceutica Sinica B

www.elsevier.com/locate/apsb
www.sciencedirect.com

ORIGINAL ARTICLE

Logic-gated tumor-microenvironment nanoamplifier enables targeted delivery of CRISPR/Cas9 for multimodal cancer therapy

Yongchun Pan[a,b,†], Xiaowei Luan[b,†], Fei Zeng[b], Xuyuan Wang[b], Shurong Qin[b], Qianglan Lu[b], Guanzhong He[b], Yanfeng Gao[b], Xiaolian Sun[c,*], Xin Han[d,*], Bangshun He[a,*], Yujun Song[b,*]

[a]*Department of Laboratory Medicine, Nanjing First Hospital, Nanjing Medical University, Nanjing 210006, China*
[b]*College of Engineering and Applied Sciences, State Key Laboratory of Analytical Chemistry for Life Science, Nanjing University, Nanjing 210023, China*
[c]*State Key Laboratory of Natural Medicines, Key Laboratory of Drug Quality Control and Pharmacovigilance, Department of Pharmaceutical Analysis, China Pharmaceutical University, Nanjing 211198, China*
[d]*School of Medicine & Holistic Integrative Medicine, Jiangsu Collaborative Innovation Center of Chinese Medicinal Resources Industrialization, Nanjing University of Chinese Medicine, Nanjing 210023, China*

Received 12 June 2023; received in revised form 24 August 2023; accepted 10 September 2023

KEY WORDS

CRISPR delivery;
Enzyme encapsulation;
Logic gate;
Hybrid material;
Hypoxia;
Gene editing;
Precise nanomedicine;
Multimodal therapy

Abstract Recent innovations in nanomaterials inspire abundant novel tumor-targeting CRISPR-based gene therapies. However, the therapeutic efficiency of traditional targeted nanotherapeutic strategies is limited by that the biomarkers vary in a spatiotemporal-dependent manner with tumor progression. Here, we propose a self-amplifying logic-gated gene editing strategy for gene/H_2O_2-mediated/starvation multimodal cancer therapy. In this approach, a hypoxia-degradable covalent-organic framework (COF) is synthesized to coat a-ZIF-8 in which glucose oxidase (GOx) and CRISPR system are packaged. To intensify intracellular redox dyshomeostasis, DNAzymes which can cleave catalase mRNA are loaded as well. When the nanosystem gets into the tumor, the weakly acidic and hypoxic microenvironment degrades the ZIF-8@COF to activate GOx, which amplifies intracellular H^+ and hypoxia, accelerating the nanocarrier degradation to guarantee available CRISPR plasmid and GOx release in target cells. These tandem reactions deplete glucose and oxygen, leading to logic-gated-triggered gene editing as well as synergistic

*Corresponding authors.
E-mail addresses: xiaolian_sun@cpu.edu.cn (Xiaolian Sun), xhan0220@njucm.edu.cn (Xin Han), bhe@njmu.edu.cn (Bangshun He), ysong@nju.edu.cn (Yujun Song).
†These authors made equal contributions to this work.
Peer review under the responsibility of Chinese Pharmaceutical Association and Institute of Materia Medica, Chinese Academy of Medical Sciences.

https://doi.org/10.1016/j.apsb.2023.09.016
2211-3835 © 2024 The Authors. Published by Elsevier B.V. on behalf of Chinese Pharmaceutical Association and Institute of Materia Medica, Chinese Academy of Medical Sciences. This is an open access article under the CC BY-NC-ND license (http://creativecommons.org/licenses/by-nc-nd/4.0/).

gene/H_2O_2-mediated/starvation therapy. Overall, this approach highlights the biocomputing-based CRISPR delivery and underscores the great potential of precise cancer therapy.

© 2024 The Authors. Published by Elsevier B.V. on behalf of Chinese Pharmaceutical Association and Institute of Materia Medica, Chinese Academy of Medical Sciences. This is an open access article under the CC BY-NC-ND license (http://creativecommons.org/licenses/by-nc-nd/4.0/).

1. Introduction

Biocomputing, an ambitious field using biological tools for information processing, displays great potential in sensing systems as well as intelligent machines, which also provides a powerful tool for biomedical implementation including bio-imaging and precision medicine[1−4]. Recent studies on molecular diagnostics and gene expression profiling have demonstrated remarkable heterogeneity within cancer[5,6]. Such tumor complexity might lead to spatial variations in the molecular makeup between subpopulations across and within disease sites or a nonsequence distribution during disease progression[7]. Therefore, specific diagnosis and treatment at all levels are demanded more accurate drug efficacy[8]. Smart materials have been developed and engineered to selectively leverage pathological cues through integrating functional groups which respond to external stimuli (such as temperature, magnetism, enzyme, reactive oxygen species, and other small molecules), guaranteeing programmed functions including logic-based biocomputation for target disease-associated biochemical hallmarks[9,10]. However, a myriad of logic gates is constructed based on the "OR" type, which actually responds to just a single stimulus, and most of the "AND" logic gate systems are activated by the intracellular and extracellular stimuli in a cascade manner, limiting tumor recognition[11,12]. Apparently, if the "AND" logic gate operations which are responsive to multiple stimuli in a simultaneous way have been achieved, a precise disease strike could be expected[13].

Beyond highly precise resolution, early treatment also gives an important determinant of survival with minimal side-effect in patients suffering from cancer[14]. Nevertheless, for targeted nanomedicine, specific pathological states including hypoxia, H^+, and GSH, have been employed as stimuli to trigger logic gates for drug delivery[15−17], yet most of such biomarkers increase as the tumor progress, implying insufficient for early antitumor therapy[18]. For example, the regions of hypoxia would ceaselessly enlarge as the tumor proliferates and dominates normal tissue[18], which suggests that a slight decrease in oxygen level hardly induces enough reductase to trigger the hypoxia-responsive approach in early-stage tumors, thereby limiting early antitumor effect. Therefore, a self-amplification strategy is an urgent need to awaken an efficient degradation for available drug delivery[19].

Herein, we developed a self-amplifying degradable nanomachine for acid "AND" hypoxia logic-gated gene editing (denoted as SALC). Beyond gene therapy, this cargo also consumed glucose and altered the oxidative stress for the combined gene/H_2O_2-mediated/starvation multimodal cancer therapy (Scheme 1). To obtain SALC, we packaged the clustered regularly interspaced short palindromic repeats (CRISPR)-associated (Cas)9 system and glucose oxidase (GOx) in amorphous zeolitic imidazolate frameworks-8 (CG@ZIF-8) first and then coated a covalent-organic framework (COF) shell containing hypoxia-sensitive azobenzene bond to load CATzyme (a DNAzyme which can cleave catalase mRNA). In the tumor microenvironment, the SALC can be degraded by weak acid "AND" hypoxia to release the CRISPR for the subsequent polo-like kinase 1 (*PLK1*, an attractive target in cancer treatments) gene editing. Such "sacrifice" also le ft Zn^{2+} to activate CATzyme for inhibiting the expression of catalase (CAT), leading to not only the effective accumulation of H_2O_2 but hypoxia intensification. In addition, the catalytic action of GOx favored a lower pH and O_2 depletion, which provided a positive feedback loop to amplify the biodegradation of SALC. Simultaneously, the GOx-based reaction produced H_2O_2 and induced glucose consumption, which contributed to the inhibition of tumor proliferation as well. This GOx-mediated biocomputing strategy offered a new paradigm to amplify gene editing in targeted cells for high therapeutic effect with limited side-effect.

2. Materials and methods

2.1. Materials

Zinc acetate and 2-methylimidazole (2-MeIM) were purchased from Sinopharm Chemical Reagent Co., Ltd. (Shanghai, China). Glucose oxidase (GOx), ethanol, and 4,4-azodianiline were purchased from Aladdin Co., Ltd. (Shanghai, China). Dimethyl sulfoxide (DMSO), and mesitylene (trimethyl benzene, TMB) were purchased from Sigma−Aldrich (Shanghai, China) Trading Co., Ltd. Phosphate-buffered saline (PBS, 10×), and Dulbecco's modified Eagle's medium (DMEM) were purchased from KeyGEN (Nanjing, China). Fetal bovine serum (FBS) was purchased from ExCell Bio (Taicang, China). Penicillin/streptomycin (P/S, 100 ×), Bovine albumin (BSA), and DAPI stain solution were purchased from Sangon Biotech (Shanghai, China) Co., Ltd. Cell Counting Kit-8 (CCK-8) was purchased from TargetMol (Boston, MA, USA). JC-1 kit, propidium iodide (PI), and calcein-AM dyes, Annexin V-FITC/PI Apoptosis Detection Kit (Cat No. 40302ES50) were acquired from Yeasen Biotechnology (Shanghai, China). 2 × Phanta Max Master Mix, ChamQ SYBR® qPCR Master Mix (High ROX Premixed), and FastPure Cell/Tissue DNA Isolation Mini Kit were purchased from Vazyme Biotech Co., Ltd. (Nanjing, China). 0.05% trypsin solution was purchased from YIFEIXUE BIOTECH (Nanjing, China). RIPA buffer and Phenylmethylsulfonyl fluoride (PMSF) were purchased from Solarbio (Beijing, China).

2.2. Preparation and characterization of CG@ZIF-8

In a typical experiment, GOx (0.25 mg/mL) and DNA plasmid were mixed in 1.0 mL of 2-MeIM (80 mmol/L) and then added into 1.0 mL of zinc acetate solution (20 mmol/L), followed by stirring for 10 min in a 5 mL glass bottle. The synthesized CG@ZIF can be obtained by centrifugation (20,000×*g*, 5 min, ambient temperature), and washing three times with deionized water. The packaging GOx and DNA plasmids can be quantified

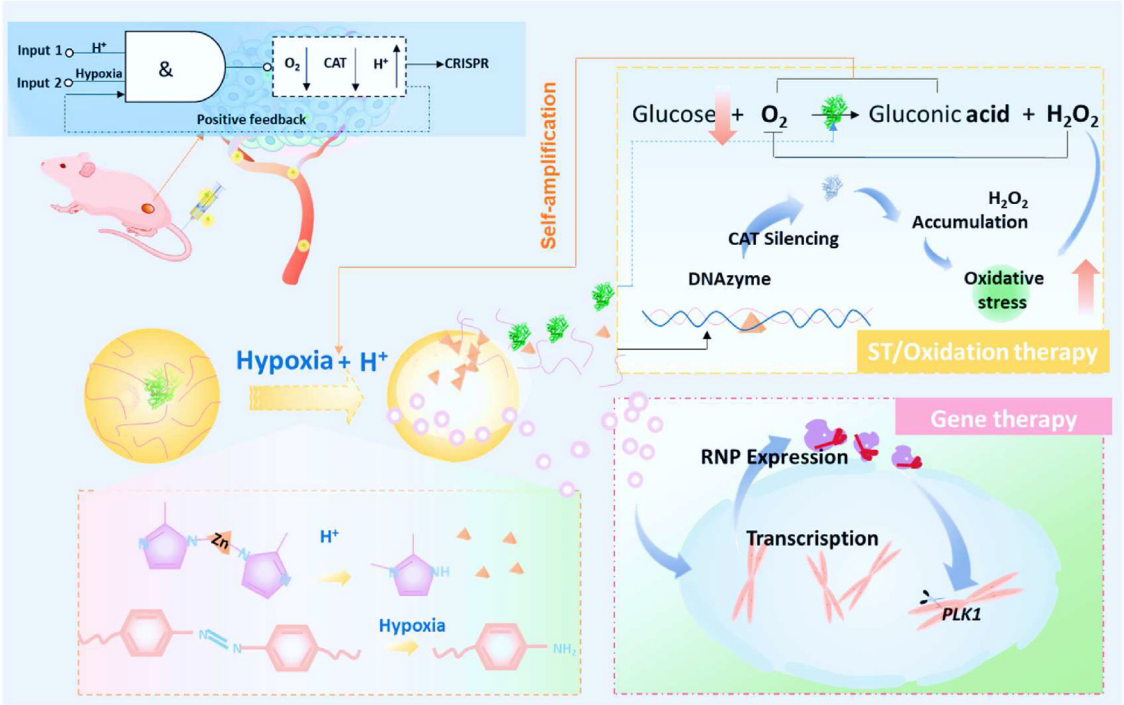

Scheme 1 Illustration of self-amplifying logic-gated gene editing system for synergistic gene/oxidation/starvation multimodal therapy.

by electrophoresis gel imaging (CliNX, GenoSens 2100, Shanghai, China).

2.3. *Preparation of SALC*

The resulting CG@ZIF-8 was dispersed in ethanol with 2,4,6-trihydroxybenzene-1,3,5-tricarbaldehyde (0.63 mg) and 4,4-azodiamine (0.945 mg). This mixture was mildly sonicated for 30 s and then stirred violently for 30 min to get CG@ZIF-azo-COF. Finally, SALC was prepared by dissolving CATzyme with CG@ZIF-azo-COF in an aqueous solution and shaken with a table concentrator overnight at 4 °C. For evaluating the adsorption efficiency of CATzyme, Cy3-labeled CATzyme (50 nmol/L) was mixed with CG@ZIF-azo-COF with a series of concentrations (0−500 μg/mL). Then, the fluorescence intensities of the obtained solutions were analyzed with a fluorescence spectrophotometer (HITACHI, F-4600, Tokyo, Japan).

2.4. *Cell culture*

4T1 (murine mammary cancer cell line), MCF-7 (human breast cancer cell line), MCF-7-EGFP, HeLa (ovarian cancer cell line), MDA-MB-231 (human triple-negative breast cancer), and A549 (non-small-cell lung cancer cell lines) were obtained from Cell Resource Center, IBMS, CAMS/PuMC (Beijing, China). The cells were incubated in DMEM containing 10% FBS and 1% P/S in an incubator with 5% CO_2 at 37 °C. All cells, if needed, were digested from the culture plates by using a 0.05% trypsin−EDTA. Mycoplasma contamination should be avoided in any of the cells.

2.5. *Cell proliferation assay*

A cell proliferation test was performed by using Cell Counting Kit-8 (CCK-8). Specifically, the 96-well plate was employed for cell culture, and all cells were seeded at a density of about 10,000 cells per well. After the adherent cells' growth, the plates were washed twice with PBS, and the same amount of medium was used with increasing concentrations of SALC ranging from 0 to 0.5 mg/mL. The CCK-8 assay was conducted according to the manufacturer's instructions. After incubation for 4 h at 37 °C, the absorption at 450 nm was recorded using a microplate reader (ThermoFisher scientific, Multiskan GO, Shanghai, China).

2.6. *Flow cytometry*

MCF-7 cells (2.5×10^4 cells per well) were treated with PBS, SALC$^{\Delta GOx}$, SALC$^{\Delta CATzyme}$, SALC$^{\Delta CRISPR}$, SALC$^{\Delta azo}$, or SALC in serum-free media. Four hours later, all cell mediums were replaced with serum-containing fresh mediums, and the cells were then incubated for 2 days. After washing with PBS, all cells were collected by treating them with trypsin−EDTA. Next, cells were washed twice with cold PBS and then resuspended cells in Binding Buffer. We added 5 μL of FITC Annexin V and 5 μL PI into the solution. Finally, 400 μL of binding buffer was added to each tub and the fluorescence of the cells (1.0×10^4 cells) was counted by using a flow cytometer (BD, FACSVerse, Sussex, NJ, USA).

2.7. *JC-1 staining*

Mitochondrial membrane potential was observed by confocal laser scanning microscope (CLSM) using the JC-1 Kit. Briefly, MCF-7 cells (2.0×10^4 cells per well, 24-well plate) were treated with control, SALC$^{\Delta Gox}$, SALC$^{\Delta CATzyme}$, ZIF-8@COF, SALC$^{\Delta CRISPR}$, and SALC in a glucose-free medium for 4 h. JC-1 staining was performed by incubation with MCF-7 cells for 20 min at 37 °C (10 μmol/L). After being washed twice according to the manufacturer's instructions, all the cells on the plates were scanned with Confocal laser scanning microscope (Olympus, FV3000, Beijing, China). Red emission of the dye in cells demonstrated a potential-

dependent aggregation in the mitochondria, while green fluorescence implied the monomeric form of JC-1, which is located in the cytosol once depolarization of the mitochondrial membrane is performed. Cells treated with 10 μmol/L carbonyl cyanide 3-chlorophenylhydrazone (CCCP) were employed as a positive control.

2.8. EGFP gene disruption assay

EGFP-MCF-7 cells were seeded into 6-well plates (~2.5×10^6 cells per well). After the cells reached 70% confluence, we replaced the medium with a 2.0 mL medium containing the SALC$^{\Delta CATzyme}$, SALC$^{\Delta GOx}$, or SALC (gRNA concentration at 100 nmol/L), respectively. Two days later, the cells were verified by using the flow cytometry analysis and fluorescent microscope (Life technologies, EVOS FL Auto, Shanghai, China). For *in vivo* assay, mice (5−6 weeks, BALB/c nude, female) were inoculated subcutaneously with EGFP-MCF-7 cells on the hind hip. When the tumors reached about 100−200 mm^3, the mice were intravenously injected with 100 μL of solution (PBS, CRISPR@ZIF-azo-COF or SALC) (Cas9 concentration at 5 μmol/L). On Day 12, the mice were euthanized and we collected the tumors for section. Such tumor sections were stained with conjugated GFP antibody and DAPI.

2.9. T7E1 assay

To determine gene editing efficiency in *PLK1* and *MHL1* genes, sgRNA targeting *PLK1* gene (5′-TACCTACGGCAAATTGTGCT-3′) and *MHL1* (5′-TCACCGTGATCAGGGTGCCC-3′) were prepared and complexed with Cas9, respectively. Cells were seeded in 6-well plates at a density of 5×10^4 cells per well and cultured overnight at 37 °C under a humidified atmosphere with 5% CO_2. Next, cells were treated with different formulations for 48 h, and genomic DNA from using a Dzup Genomic DNA Isolation Reagent. The sgRNAs targeting the *PLK1* and *MHL1* were amplified using the High-Fidelity PCR Master Mix (Sangon Biotech Co., Ltd., Shanghai, China) with the corresponding PCR primers. Indel efficiency was detected using a T7 Endonuclease I kit (Vazyme Biotech Co., Ltd., China), and indel event frequencies were calculated using ImageJ (National Institutes of Health, Bethesda, MD, USA).

2.10. RT-PCR

After being treated with different formulations, the total RNA was isolated from the cells using TRIZOL reagent, followed by cDNA preparation using reverse transcriptase (Vazyme Biotech Co., Ltd.) according to the manufacturer's instructions. For target gene (CAT and GAPDH) amplification, each primer was provided by Sangon Biotech (Shanghai) Co., Ltd., and the RT-PCR was performed with SYBR Green I with primer sequences as follows:

F-CAT, 5′-TGGAGCTGGTAACCCAGTAGG-3′;
R-CAT, 5′-CCTTTGCCTTGGAGTATTTGGTA-3′;
F-GAPDH, 5′-GGAGCGAGATCCCTCCAAAAT-3′;
R-GAPDH, 5′-GGCTGTTGTCATACTTCTCATGG-3′.

2.11. Western blotting

After being treated with different formulations, cells were lysed with RIPA buffer (1 mmol/L PMSF) for protein collection. For quantification, the BCA assay kit was employed according to the manufacturer's instructions (P0010S, Beyotime Biotechnology). Equal amounts of protein (50 μg) diluted in water containing 5 × loading buffer were loaded onto an SDS-PAGE gel. Afterward, we separated proteins by electrophoresis at 120 V for 120 min, and such proteins were transferred to a PVDF membrane in 1 × Tris-glycine Native Buffer with 10% methanol at 4 °C for 120 min. After being blocked with QuickBlock™ Blocking Buffer (P0220, Beyotime Biotechnology) to inhibit nonspecific binding, the membrane was incubated at 4 °C with the corresponding primary antibody. Next day, Horseradish peroxidase (HRP)-conjugated antibodies (reactive with rabbit) were applied as secondary antibodies to incubate with the membranes at RT for 1 h. After reacting with the TMB chromogenic solution, the PLK1 protein was visualized using Gel Imager (CliNX, GenoSens 2100, Shanghai, China).

2.12. Animal study

All animal experiments were conducted in compliance with the guidelines approved by the Animal Ethics Committee of Nanjing University (Approval No. IACUC-2003082). Cy7-labeled SALC (Cy7-SALC) was obtained for *in vivo* monitoring. Mice (5−6 weeks, BALB/c nude, female) were inoculated subcutaneously with MCF-7 cells on the hind hip. After 2-week incubation, mice were intravenously administered 100 μL of Cy7-SALC (100 μg/mL) into the tail vein. The accumulation of SALC was obtained periodically using *in vivo* fluorescence microscopy (IVIS Spectrum *In Vivo* Imaging System, PerkinElmer) using wavelength for Cy7 (745/800 nm).

Besides, we also prepared 30 MCF-7 tumor-bearing nude mice and randomly divided them into 6 groups. While the tumor volume reached 100 mm^3, the antitumor efficacy was monitored by recording the changes in the tumor volume after i.v. injection of PBS, SALC$^{\Delta GOx}$, SALC$^{\Delta CATzyme}$, SALC$^{\Delta CRISPR}$, SALC$^{\Delta azo}$, and SALC (100 μg/mL) for 14 days. All entities were intravenously injected every 2 days. Tumor volumes were calculated according to Eq. (1):

$$\text{Tumor volume} = 0.5\ L \times (W)^2 \quad (1)$$

where L and W denote the longest and shortest diameters of a tumor, respectively.

2.13. Histology

Tumor tissues and major organs were extracted from euthanized mice and incubated in 4% paraformaldehyde solution at 4 °C for fixation. Next, we embedded the collected tissues in paraffin blocks and sliced them into 5 μm thick sections. For deparaffinization, the paraffin-embedded sections needed to be soaked in xylene three times and simultaneously hydrated with decreasing amounts of ethanol. For H&E staining, we soaked the sections in hematoxylin and eosin solution, sequentially. And the sections were sandwiched between coverslips and the mounting buffer for observation under an optical microscope. As for immunofluorescence staining, two antibodies (*i.e.*, primary and secondary antibodies) were applied to visualize the target proteins. Subsequently, the obtained sections were immersed in a mounting medium containing DAPI for better observation using a fluorescence microscope (EVOS FL Auto).

2.14. Tumor-specific gene editing

To verify the selective gene editing, mice (5−6 weeks, BALB/c, female) were inoculated subcutaneously with 4T1 cells on the

hind hip. Since 4T1 is a murine cancer cell line, it shares some *MHL1* gene sequences with a murine hepatic cell for comparison. After 2-week incubation, the mice were intravenously administered SALC into the tail vein. On Day 10, the mice were euthanized. and the tumor tissues were collected, sliced, or lysed to evaluate the levels of *MHL1* disruption by immunofluorescence (protein) or deep sequencing (gene). Here, the target gene locus is shown as follows: TCACCGTGATCAGGGTGCCC.

2.15. Statistics analysis

Data were presented as means ± SD ($n = 3$). For the representativeness of the qualitative images shown, at least two experiments were carried out in duplicate. For differences between the two groups, $^{**}P < 0.01$ was considered significant while $^{***}P < 0.001$ was considered highly significant.

3. Results and discussion

3.1. The design of a dual-responsive logic system

We packaged CRISPR plasmid and GOx in acid-degraded amorphous zeolitic imidazolate frameworks-8 (CG@ZIF-8) with a diameter of 50 nm according to the previous description with slight modification[20] (Fig. 1A and B). Thereafter, building blocks of COF, 4,4-azodiaminobenzene (AD) and 1,3,5-triformyl-2,4,6-trihydroxybenzene (TP) were added for the growth of azo-containing responsive COFs on the CG@ZIF-8 (denote as CG@ZIF-azo-COF or SALC$^{\Delta CATzyme}$) *via* the Schiff-base reaction. The transmission electron microscopy (TEM) demonstrated that building blocks with high concentration would lead to severe aggregation (Fig. 1B), and thus the TP was set at 1.0 mg/mL. Finally, after incubation with the resulting nanoplatform, CATzyme was loaded onto the surface and formed a self-amplifying acid "AND" hypoxia logic-gated CRISPR system delivery (SALC) with about 60 nm (Fig. 1C). The zeta potentials revealed that a negative charge could be observed after co-loaded CRISPR plasmid and GOx different with the positive charge of a-ZIF-8, and the positive value of CG@ZIF-azo-COF was weakened upon the addition of CATzyme (Fig. 1D). Meanwhile, the clear emergence of absorption peak at about 1453 cm^{-1} in the FTIR spectroscopy further indicated the formation of the COF shell (Fig. 1E). To further confirm the successful encapsulation of plasmid and GOx, gel electrophoresis analysis was employed. And the results displayed that both plasmid (stained with gel red) and GOx protein (stained with Coomassie brilliant blue) blottings were evidently discovered in the CG@ZIF-8 group after acid treated, while no signal was detected in the supernatant (Fig. 1F). Similar results also were obtained by a fluorescence spectrophotometer (Supporting Information Supporting Information Fig. S1). Besides, the ratio of CG@ZIF-azo-COF to CATzyme was optimized by recording the excess CATzyme, and we eventually adopted 100 μg/mL CG@ZIF-azo-COF to absorb CATzyme with 50 nmol/L for further use according to Fig. 1G.

Next, we investigated the multiple functions of the SALC. First, H_2O_2 producing capacity was measured by monitoring the change of UV−Vis absorption against the substrate 3,3′,5,5′-tetramethylbenzidine (TMB) (Fig. 2A). As shown in Fig. 3B and Supporting Information Supporting Information Fig. S2, the absorption at 652 nm was increased upon the increase of glucose, indicating that the H_2O_2 generation was dependent on the catalytic activity of GOx in SALC. Interestingly, the glucose oxidase activity after coating with a-ZIF-8@COF and CATzyme demonstrated much weaker than that of free GOx (Fig. 2C, Supporting Information Supporting Information Fig. S3), which probably stemmed from that such shells damaged the diffusion efficiency of substrates to attach the GOx inside. Thereby, when the acid environment degraded the SALC, the confine of GOx was lifted and H_2O_2 was generated more easily. Secondly, the SALC can reduce environmental pH by GOx-catalyzed aerobic oxidation of glucose. As the concentration of glucose increases, the produced gluconic acid is enhanced, and the pH value decreases could be monitored by a pH meter (Fig. 2D). Thirdly, our nanosystem demonstrated acid-responsive Zn^{2+} releasing properties due to the easily protonated imidazole nitrogen. As seen in Fig. 2E, the Zn^{2+} release rate rapidly raised as the pH reduced. And in the medium with high glucose, the increased H^+ from glucose oxidation also contributed to SALC degradation and Zn^{2+} release. Such ions can serve as effective cofactors for CATzyme to completely cleave the CAT RNA[21], and the cleavage efficiency increased in a Zn^{2+} concentration-dependent manner (Supporting Information Supporting Information Fig. S4). Last, O_2 depletion was real-time measured by a Foxy Fospor-R O_2 probe in different pH buffers containing glucose. As expected, SALC in a lower pH buffer consumed more O_2 within 60 min (Fig. 2F), and the O_2 consumption became faster with the addition of glucose in a concentration-dependent manner (Supporting Information Supporting Information Fig. S5). Besides, we also investigated the SALC-induced hypoxia aggravation both *in vitro* and *in vivo*. Under the combined effect of GOx and CATzyme-triggered catalase silence, the fluorescence signal achieved maximum, suggesting that our system can efficiently exhaust the O_2 and lead to significantly enhanced tumor deoxygenation (Supporting Information Supporting Information Fig. S6). Additionally, the signal of intratumoral hypoxia-inducible factor-1 (HIF-1) significantly improved after i.v. injection of SALC (Fig. 2G and H), implying the hypoxia self-amplifying of our approach.

3.2. A positive feedback loop for amplifying gene editing

To prove the hypoxia "AND" H^+ responsiveness of SALC, we used sodium hydrosulfite (SDT, an analog of hypoxia-induced azoreductase)[22,23] and sodium acetate buffer (pH = 5.0) as two signal inputs. Since H^+ can dissolve ZIF-8 and azoreductase would catalyze the decomposition of azobenzene in COF, the CRISPR plasmids can release from the nanoplatform only where there coexisted SDT and acidic environment (Fig. 3A and Supporting Information Supporting Information Fig. S7). To observe the degradation easily, TEM was conducted for SALC after different treatments. As shown in Fig. 3B, unlike the H^+ or SDT group where the outline of SALC can still be found, the SDT+ H^+ group only left tiny pieces that presumably were benzenamine materials. Such successfully verifying the SDT and H^+ response abilities laid a foundation for the construction of AND logic gate in the following study.

To investigate the logic gate-regulated gene editing performance in living cells, we first examined the transfection efficacy of gene expression by mixing MCF-7 with SALC where the plasmid expression vectors coded green fluorescent protein gene. As shown in Supporting Information Supporting Information Fig. S8, obvious green fluorescence signals were observed in both CRISPR-loaded zeolitic imidazolate framework-azo-covalent organic framework (CRISPR@ZIF-azo-COF) and SALC groups,

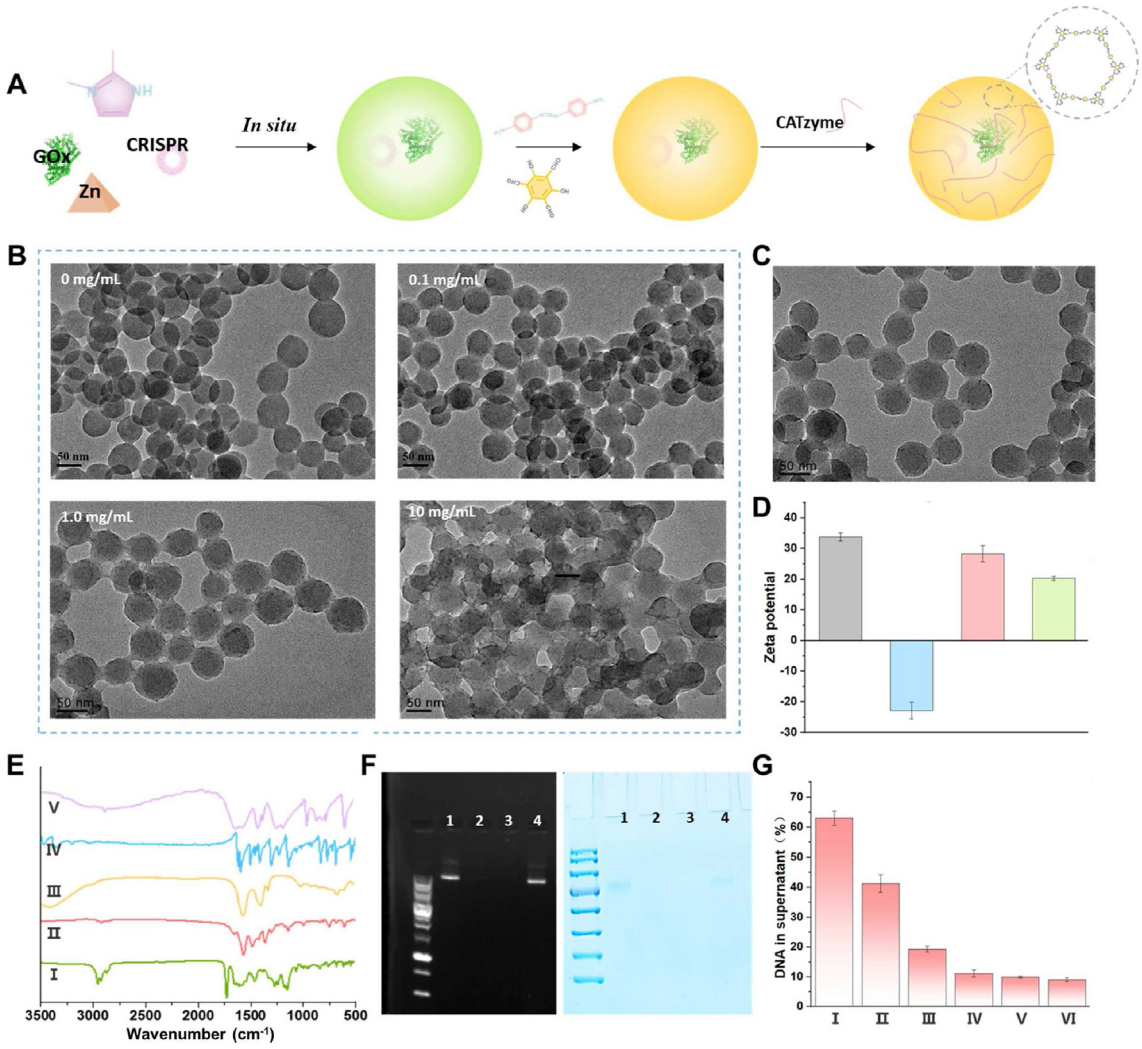

Figure 1 The construction and characterization of SALC. (A) Schematic diagrams illustrating the fabrication of the SALC. (B) TEM images of ZIF-8 coated with different COF precursors, as summarized by the illustration. (C) TEM images of the resulting SALC. Scale bar: 50 nm. (D) Zeta potentials of a-ZIF-8, CG@ZIF-8, CG@ZIF-azo-COF, and SALC (from left to right). (E) FTIR spectra of I: a-ZIF-8, II: 2,4,6-triformylphloroglucinol, III: 4′,4′-diaminoazobenzene, IV: a-ZIF-8@COF. (F) Agarose and SDS-page gel shift for revealing the encapsulation efficiency of DNA plasmid and GOx. 1, control; 2, the residual CRISPR-coded plasmid or GOx in the supernatant after encapsulation; 3, a-ZIF-8 nanostructures; and 4, ZIF-8 after acid degradation. (G) Supernatant CATzyme after incubation with different concentrations of CG@ZIF-azo-COF. The fixed concentration of CATzyme was 50 nmol/L, and the concentrations of CG@ZIF-azo-COF were I: 10, II: 20, III: 50, IV:100, V:200, and VI: 500 μg/mL, respectively. Data are presented as mean ± SD ($n = 3$).

and more EGFP expression can be recorded in SALC group due to its H^+ and hypoxia amplification. Next, to determine the gene editing efficiency for convenience, the CRISPR-Cas9 was constructed to target the coding region of *EGFP* in MCF-7 cell line expressing a destabilized EGFP protein (EGFP-MCF-7). As a proof-of-concept, we construct a 2-input Boolean AND gate to regulate gene editing where acid and hypoxia served as the inputs (Fig. 3C). Fig. 3D illustrated *EGFP* gene was knockout upon delivering *EGFP*-targeted CRISPR by SALC in the acid and hypoxia environment, as demonstrated by a significant decrease in the EGFP-MCF-7 cells fluorescence. And flow cytometry revealed that the cells reduced significant fluorescence only in the acid + hypoxia group, which achieved approximately 32% (Fig. 3D and E), suggesting that the logic gate functioned as anticipated. In addition, once we replaced the azo-COF with an azo-free one (CRISPR@ZIF-COF), the CRISPR@ZIF-COF hardly induced a significant difference in acid and hypoxia environment, which confirmed the response characteristic of hypoxia originated from azobenzene (Supporting Information Supporting Information Fig. S9).

Based on the logic gate-response characteristic of CRISPR@ZIF-azo-COF, we then tested the 'positive feedback loop' concept by comparing the CRISPR@ZIF-azo-COF with SALC in the different oxygen-content environments (Fig. 3F). Under normoxic conditions, CRISPR@ZIF-azo-COF cannot be degraded and the hypoxiainduced by SALC still hardly led to enough nitroreductase for CRISPR releasing to edit gene whereas enough nitroreductase appeared under severe hypoxia (1% O_2), contributing to great reduced fluorescent signals in both of them exhibited (Fig. 3G, Supporting Information Figs. S10 and S11). We discovered that the distinctive difference between CRISPR@ZIF-azo-COF and SALC only came about under a

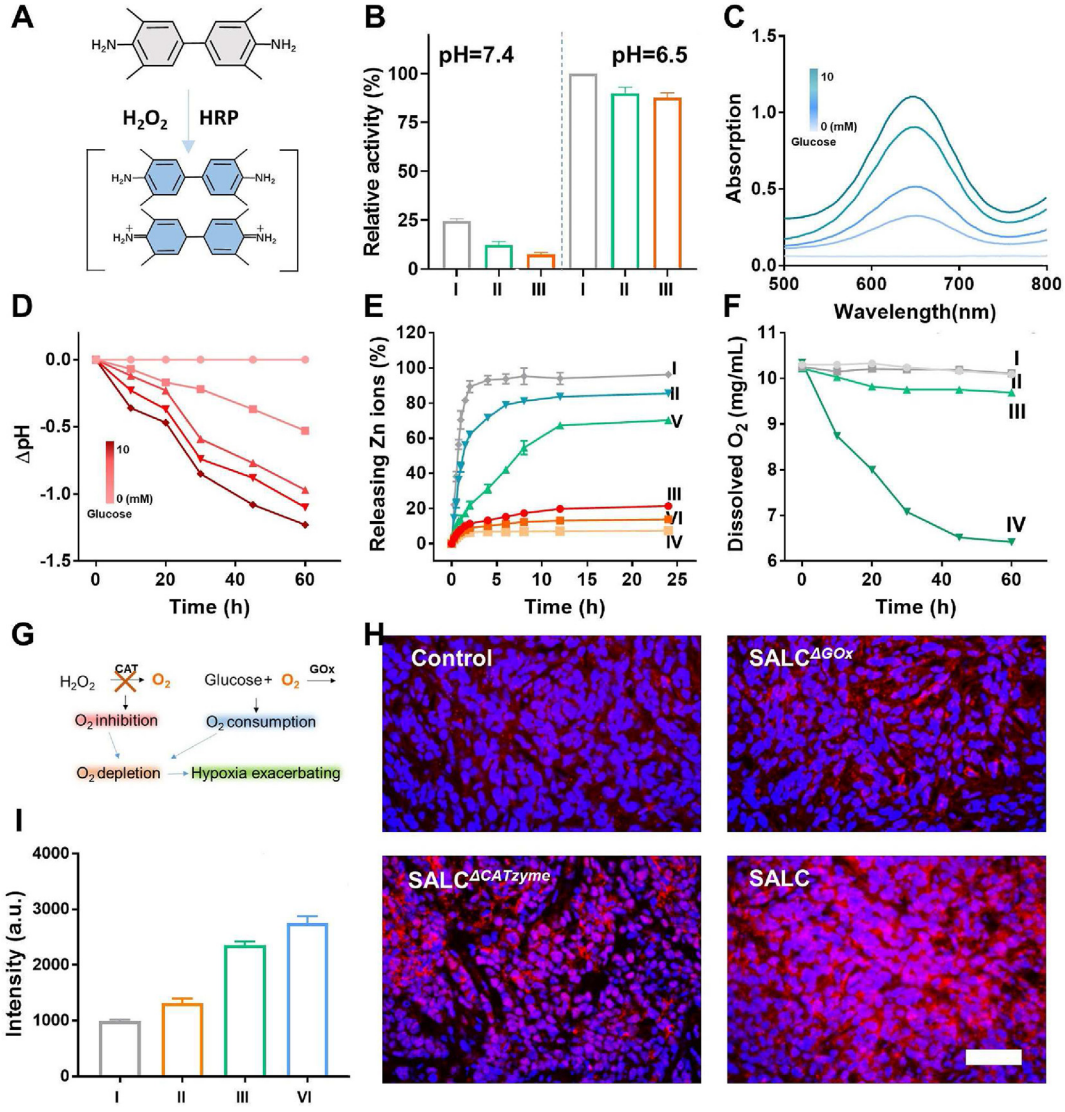

Figure 2 Acids and hypoxia amplifying by SALC. (A) The reaction of 3′,3′,5,5′-tetramethylbenzidine (TMB) with H_2O_2 to generate blue resorufin products for H_2O_2 detection. (B) Relative GOx activity of SALC in different pH. I: free GOx, II: CG@ZIF-azo-COF, III: SALC. (C) The absorption spectra of oxidized TMB catalyzed by SALC in the presence of different concentrations of glucose. (D) Time-dependent pH values of the buffer containing SALC with different concentrations (0, 1.0, 2.5, 5.0, and 10 mmol/L). (E) Releasing Zn^{2+} from SALC under different environments: I: pH = 4.5, II: pH = 5.5, III: pH = 6.5, IV: pH = 7.4, V: pH = 6.5+glucose, and VI: pH = 7.4+glucose. (F) O_2 depletion rates in different pH-buffered saline containing SALC in the presence of 10 mmol/L glucose. I: control in pH = 7.4, II: control in pH = 6.5, III: SALC in pH = 7.4, IV: SALC in pH = 6.5. (G) Schematic illustration of the experimental procedures for tumoral hypoxia evaluation. (H) Representative tumoral hypoxia-inducible factor-1(HIF-1) immunofluorescence images. Scale bar: 200 μm. (I) Quantification of tumor hypoxia level based HIF-1 staining for different treatment groups. I: control, II: SALC$^{\Delta GOx}$, III: SALC$^{\Delta CATzyme}$, IV: SALC. Data are presented as mean ± SD (n = 3).

"moderate" hypoxia environment (5% O_2). Such phenomenon was occasioned by that relatively low azoreductase, which cannot completely damage the COF of CRISPR@ZIF-azo-COF group, was enhanced by the SALC. To be specific, SALC can deplete O_2 and reduce pH in the environment as mentioned above, which amplified the "sacrifice" to release CRISPR, and therefore, greater change in EGFP was observed than that of CRISPR@ZIF-azo-COF or CG@ZIF-azo-COF (Supporting Information Figs. S10 and S11, and Supporting Information Supporting Information Fig. S12). We further evaluated the *in vivo* self-amplification of CRISPR using MCF-7-EGFP tumor-bearing mice as models. After ten days, approximately 25% of the cells displayed no EGFP expression in the SALC-treated mice, while no loss of EGFP signal or less fluorescence was recorded in the control group or the one treated with CRISPR@ZIF-azo-COF (Fig. 3H, Supporting Information Supporting Information Fig. S13), demonstrating the available self-amplification of gene editing *in vivo*.

3.3. *Multimodal anticancer in vitro*

Inspired by the self-amplified logic-gated *EGFP* gene editing, we next targeted *PLK1* to knockout for anticancer (Fig. 4A). The cells in all groups were cultured in a 5% O_2 atmosphere to better investigate the positive feedback-mode anticancer. Similar to the

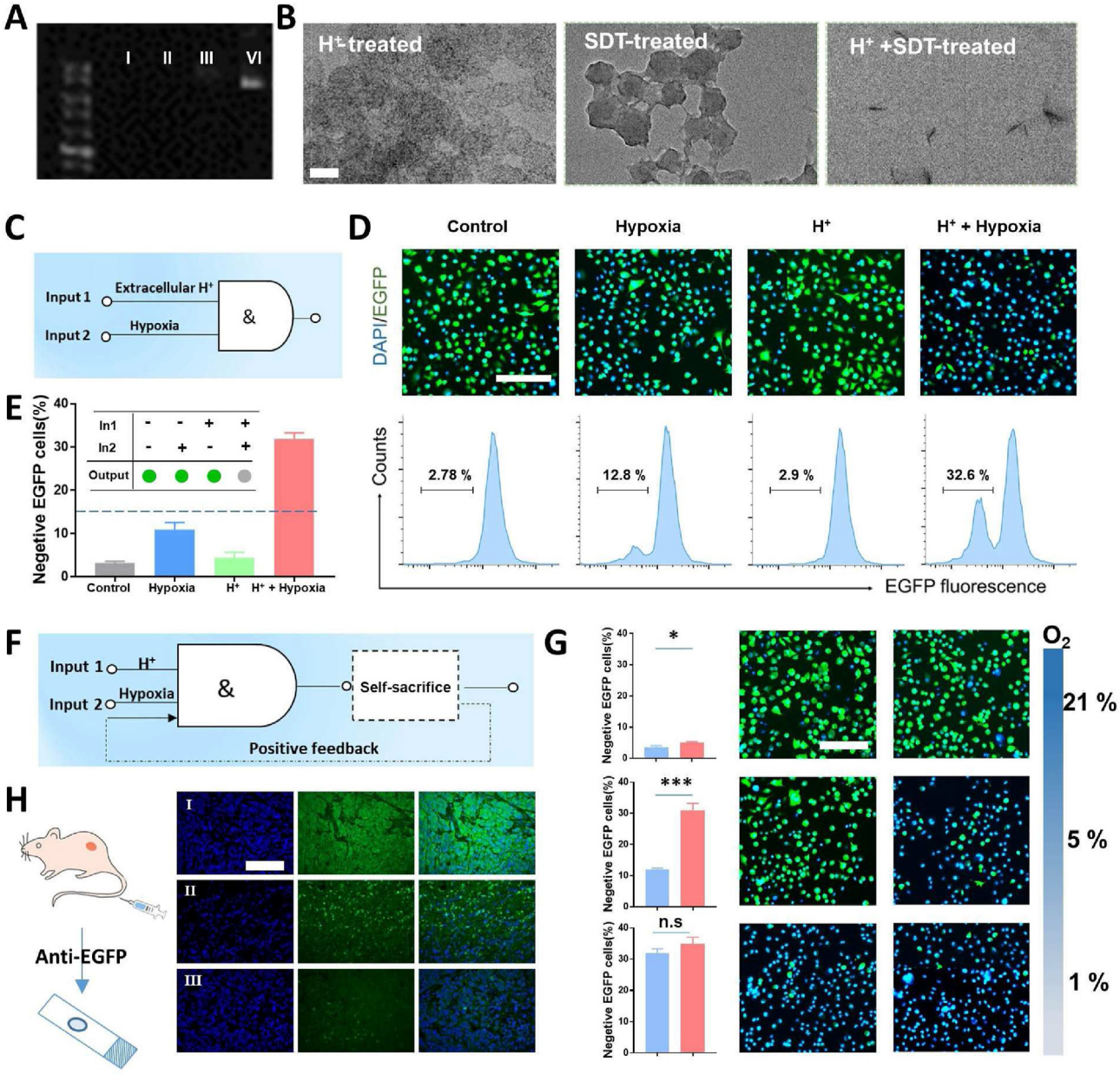

Figure 3 Self-amplifying logic-gated nanoCRISPR system for *EGFP* disruption. (A) Agarose gel of releasing CRISPR/Cas9 plasmid. I: no input (0,0), II: acid input (1,0), III: SDT input (0,1), IV acid and SDT co-input (1,1). (B) TEM images of SALC after different treatments. Scale bar: 50 nm. (C) Schematic representation of the AND logic gate. (D) Fluorescence microscopy images and the corresponding flow-cytometry analysis of MCF-7-EGFP cells incubated with CRISPR@ZIF-azo-COF after different treatments. Blue: nuclei stained with DAPI; green: EGFP. Scale bar: 200 μm. (E) Negative EGFP cell ratio after different treatments. In1 = acid, In2 = hypoxia. Data are presented as mean ± SD ($n = 3$). (F) Schematic representation of the self-amplifying AND logic gate. (G) The percentages of EGFP negative cells and the fluorescence microscopy images of MCF-7-EGFP in CRISPR@ZIF-azo-COF (blue, left in the figure), or SALC (red, right in the figure)-containing culture medium under different oxygen concentrations. Scale bar: 200 μm. (H) *In vivo* delivery of different systems into MCF-7-EGFP xenograft tumors in nude mice. $^{*}P < 0.01$; $^{***}P < 0.001$; n.s., not significant. Tumor sections were collected 14 days after i.v. injection of I: PBS, II: CRISPR@ZIF-azo-COF, and III: SALC, respectively. Scale bar: 200 μm.

control group, acid, and hypoxia treatment had no significant effect on the gene editing of *PLK1*. As a comparison, acid "AND" hypoxia logic gate could reduce the expression of the PLK1 protein, and the least protein level appeased in the SALC group due to the self-sacrificially degradable nanomachine for the amplification of CRISPR releasing (Fig. 4B). To better verify the gene editing, the corresponding insertion/deletion (indel) was detected by T7E1 analysis. The results showed that the highest efficiency was observed in the SALC group, which reached 23.7% (Fig. 4C). Meanwhile, representative mutant alleles harboring indel in the SALC group were further confirmed in Fig. 4D.

Next, we further explored the multimodal anticancer of SALC (Fig. 4E). As expected, the released Zn^{2+} from a-ZIF-8 in an acidic environment could assist CATzyme to cleave CAT mRNA

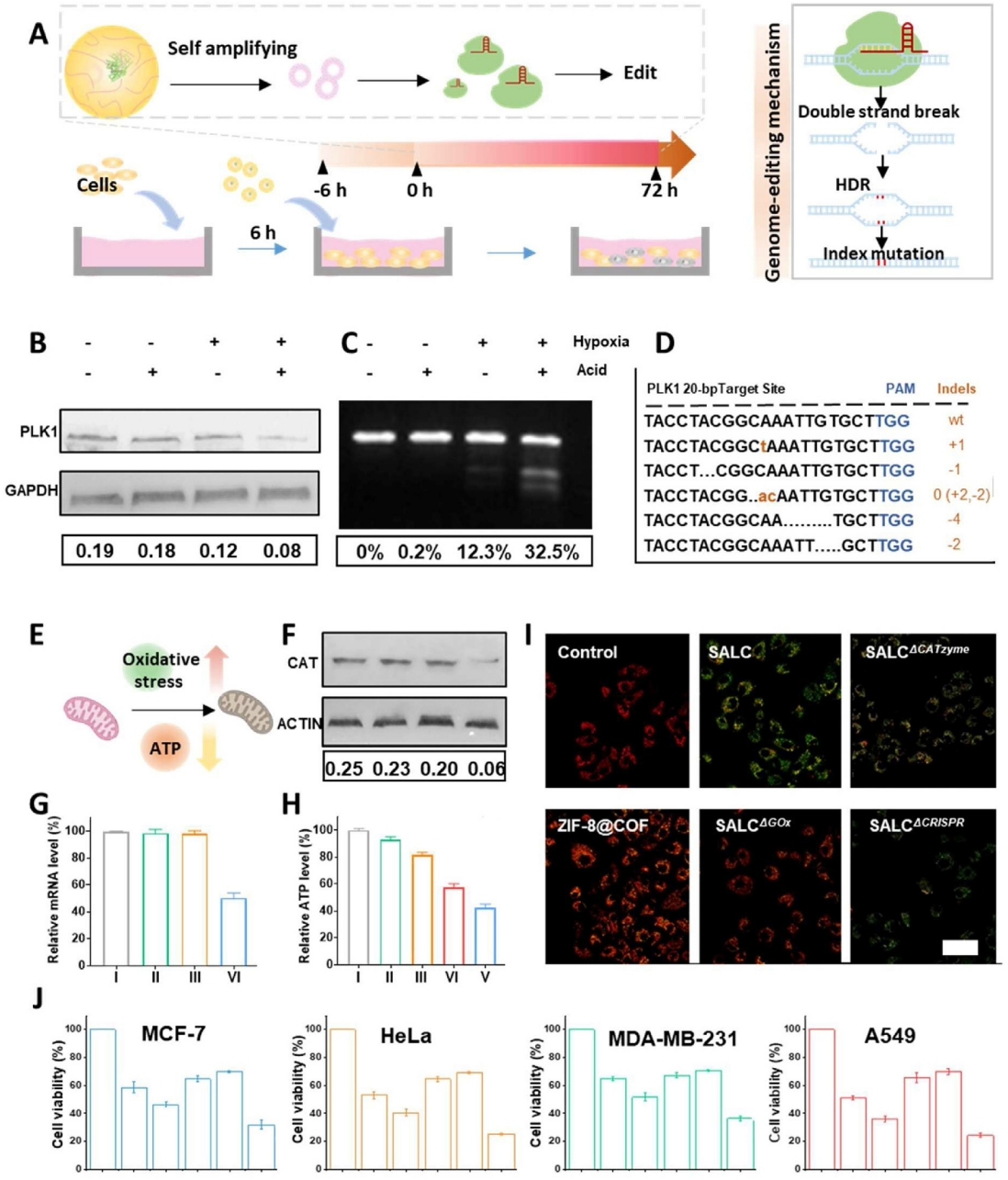

Figure 4 The potential multimodal anticancer mechanism of SALC. (A) Illustration of genome editing in MCF-7 cells. (B) Western blot and (C) T7E1 analysis of *PLK1* gene editing after different treatments. (D) Representative DNA sequencing sequences of *PLK1* locus after incubation with SALC under acid and hypoxia environment. (E) Illustration of the mitochondria injury induced by SALC. (F) Western blot and (G) RT-PCR analysis of the catalase silencing. From left to right: control, free CATzyme, SALC$^{\Delta CATzyme}$, SALC. (H) The ATP level in MCF-7 after different treatments. I: control, II: ZIF-8@COF, III: SALC$^{\Delta GOx}$, IV: SALC$^{\Delta CATzyme}$. V: SALC. (I) Mitochondrial membrane potential measured by JC-1 dye. Scale bar: 25 μm. (J) Cytotoxicity profiles of various formulations to MCF-7, HeLa, MDA-MB-231, and A549. (From left to right: control, SALC$^{\Delta GOx}$, SALC$^{\Delta CATzyme}$, SALC$^{\Delta CRISPR}$, SALC$^{\Delta azo}$, and SALC). The cells were cultured in a hypoxia environment (5% O_2). Data are presented as mean ± SD ($n = 3$).

and decrease the protein expression, which cut off the pathway of H_2O_2 decomposition by CAT and was beneficial for tumor hypoxia. Indeed, as shown in Fig. 4F and G, a significant down-regulation of CAT mRNA and protein expression were observed in SALC group but not in the CATzyme, and SALC$^{\Delta CATzyme}$ groups, as measured by both quantitative real-time polymerase chain reaction (RT-PCR) analysis and Western blot. Meanwhile, since glucose would be consumed by SALC, the glycolysis of tumor cells was effectively inhibited as proved by the lower ATP level (Fig. 4H). Besides, the catalytic oxidation of glucose also enhanced H_2O_2 content and altered the oxidative stress level in living cells (Supporting Information Supporting Information

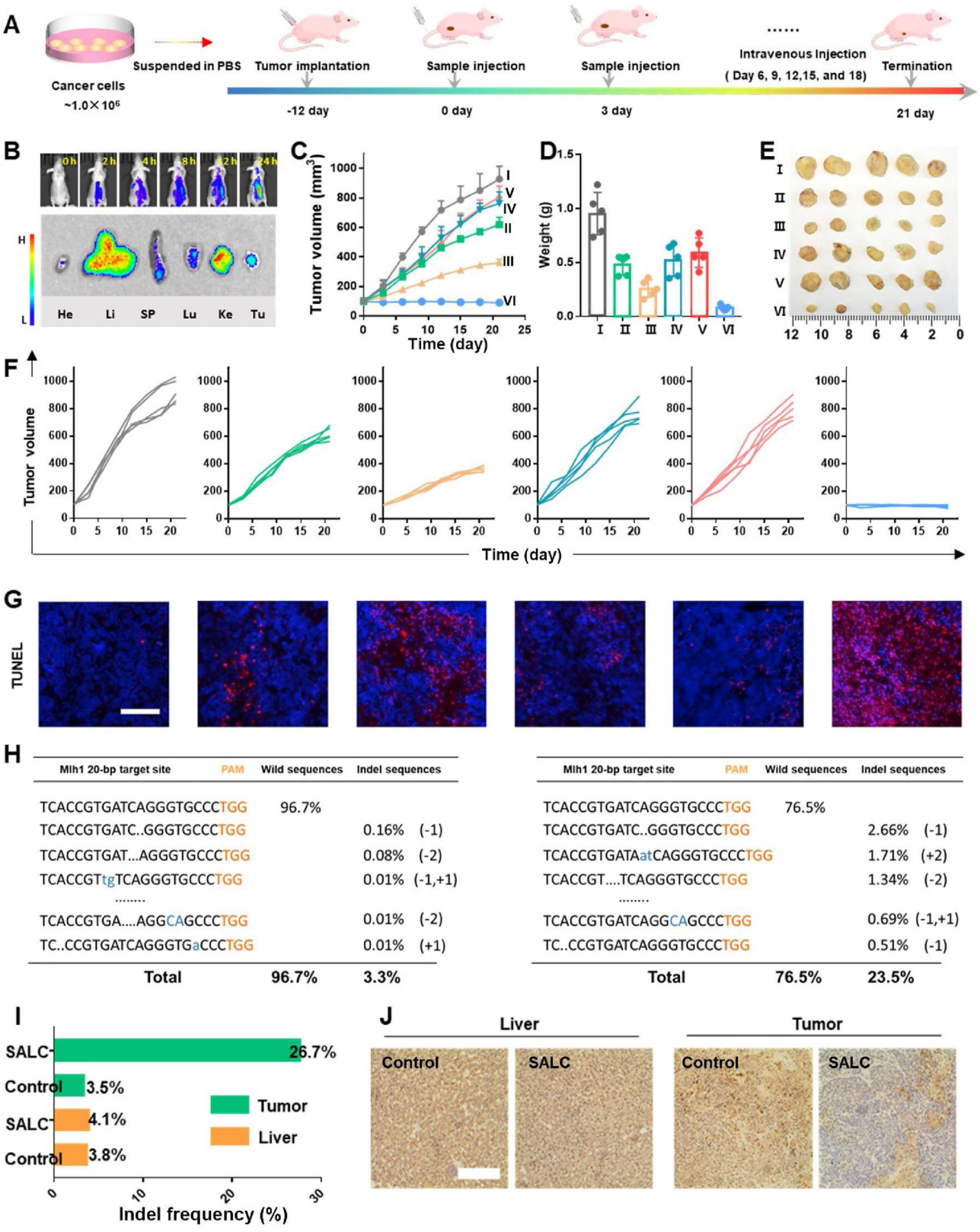

Figure 5 *In-vivo* antitumor effect of SALC. (A) Schematic diagram displaying the establishment of the MCF-7 tumor-bearing mice model and the treatment regimen. (B) Biodistribution of SALC at different time points and its distribution in main organs at 24 h. (C) Tumor-volume curves and (D) tumor weights after different treatments. Data are presented as mean ± SD ($n = 5$). (E) Photographs of the collected tumors in different treatment groups. (F) Specific tumor−volume curves of each group. I: PBS, II: SALC$^{\Delta GOx}$, III: SALC$^{\Delta CATzyme}$, IV: SALC$^{\Delta CRISPR}$, V: SALC$^{\Delta azo}$, and VI: SALC. (G) TUNEL staining fluorescence images of tumor sections after various treatments. Scale bar: 200 μm. (H) NGS analysis of indel percentage after SALC treatment in liver and tumor. (I) Comparison of the gene editing in tumor and liver tissues. (J) Immunohistochemistry analyses of MHL1 in liver and tumor sections. Scale bar: 200 μm.

Fig. S14). As shown by the mitochondrial membrane potential assay kit, our nanomachine brought the lowest mitochondria transmembrane potentials on the common effect of decreased ATP and increased H_2O_2 (Fig. 4I), which supported the apoptosis of cancer cells.

Motived by the logic-gated gene editing and mitochondria injury of SALC, we then corroborated the anticancer potential *in vitro*. As shown in Supporting Information Fig. S15, most of MCF-7 cells were alive even the SALC reached 100 μg/mL. As anticipated, the phytoactive is presented in an acid-"AND"-hypoxia-dependent manner (Supporting Information Fig. S16). To further examine the mechanism, the cells were exposed to a 5% O_2 environment and co-cultured with SALC$^{\Delta GOx}$, SALC$^{\Delta CATzyme}$, SALC$^{\Delta CRISPR}$, SALC$^{\Delta azo}$, and SALC, respectively ($^{\Delta}$ denoted as deletion, for example, SALC$^{\Delta GOx}$ stood for SALC lacking GOx). Supporting Information Fig. S17 revealed the outstanding therapeutic efficacy of SALC due to the combination of enhanced oxidative stress, starvation therapy, as well as positive feedback logic-gated genome editing, and we discovered that each part of SALC was indispensable for effectively killing cells. To test the universality of anti-cancer, other cancer cell lines, HeLa, MDA-MB-231, and A549, were employed to examine their tolerance to the SALC, and similar results were observed as shown in Fig. 4J, implying the broad-spectrum anticancer of our nanomachine.

3.4. *Self-sacrificially degradable nanomachine for tumor-specific gene editing in vivo*

Encouraged by the high cytotoxicity of SALC in cellular experiments, we studied its antitumor effect *in vivo via* systemic administration (Fig. 5A). As shown in Fig. 5B, the Cy7 fluorescence signal continuously increased at the tumor site in 24 h after administration of Cy7-labeled SALC, suggesting the available accumulation of our nanoplatform in a solid tumor, which was presumably attributed to the enhanced permeability and retention (EPR) effect of nanoparticles. Afterward, 30 mice bearing MCF-7 tumors of about 100 mm^3 were randomly divided into 6 groups for injection of different formulations. Compared with SALC groups, other groups exhibited weaker anticancer effects as shown in Fig. 5C−F. Besides, TUNEL and H&E staining (Fig. 5G and S18) confirmed that SALC groups induced much more severe apoptosis than others, which indicated the significant antitumor effect of our strategy. In addition, no obvious difference was observed in the body weight of each group (Supporting Information Fig. S19), and the H&E staining analysis also implied no significant side effects to the major organs after i.v. of SALC (Supporting Information Fig. S20). Taken together, our designed SALC demonstrated a remarkable therapeutic outcome and negligible side effects, which is potential for future clinical practice.

Subsequently, we investigated the mechanism of the combined therapy *in vivo*. First, we evaluated the common effects of GOx, CATzyme, and CRISPR-Cas9 on the ROS level. As shown in Supporting Information Fig. S21, SALC, and SALC$^{\Delta CRISPR}$ displayed the highest signals of DCF in tumor tissue than that of others, and without the CATzyme for CAT silence (Supporting Information Fig. S22), the ROS level in SALC$^{\Delta CATzyme}$ group was decreased. Next, the gene editing efficiency of SALC was analyzed *in vivo*. Similar to the groups treated with PBS, tumors receiving SALC$^{\Delta CRISPR}$ and SALC$^{\Delta azo}$ also expressed high PLK1 protein, while the protein in SALC$^{\Delta GOx}$, SALC$^{\Delta CATzyme,}$ and SALC was limited obviously, and the least protein in SALC group owing to its self-amplification of H^+ and hypoxia (Supporting Information Fig. S23). Such gene disruption was further confirmed by the T7E1 Kit (Supporting Information Fig. S24) and the representative sequencing sequences of *PLK1* locus were demonstrated in Supporting Information Fig. S25.

An ideal intelligent nanomachine is expected to complete tasks according to external information in the targeted location[24]. In this work, we need that gene editing to be tumor-specific, and other locations, especially the normal organs such as the liver, should avoid the unwanted side effects. Due to no or less expression of PLK1 in adult cells, the SALC was designed to target a widely expressed gene[25], *MHL1*, for readily testing the spatially controlled gene editing. The negligible indel event frequency in the liver was observed in T7E1 analysis, while high gene disruption efficiency was found in tumor (Supporting Information Fig. S26). To further confirm the "on-target" gene editing of our strategy, we measured the mutation of the *MHL1* locus both in the tumor and in liver tissues by DNA sequencing (Sanger sequencing analysis). As shown in Fig. 5H−I, the SALC treatment induced significant mutations in tumor, but failed to cause mutations in the liver. Besides, great differences in MHL1 protein expression can be observed in tumors, while no significant change was found in liver (Fig. 5J), suggesting the tumor-specific gene editing of SALC.

4. Conclusions

The implementation of CRISPR-based genome editing machinery *in vivo* is of significance for disease therapy and beyond due to their simplicity and accuracy[26−28]; however, their clinical application still faces substantial challenges by the difficulty in delivering to the relevant tissues[29]. Recent innovations in nanomaterials science expand the abundant toolboxes for CRISPR vehicle, and a tremendous amount of attempt has been devoted to the designs of smart cargos[30−36]. Distinguish from previous reports, this strategy contains "AND" logic gates for responding to pathological markers (H^+ and hypoxia), which improves treatment efficacy and mitigates genotoxicity. Besides, the co-delivery of GOx provides a positive feedback loop to amplify the CRISPR release for the combined Gene/H_2O_2-mediated/starvation multimodal antitumor effect. We expect this biomaterial engineering approach for spatial control of CRISPR delivery will be expanded toward smart nanodesign for precision medicine.

In summary, we have proposed a self-amplifying gene editing strategy for gene//H_2O_2-mediated/starvation multimodal cancer therapy, where a hypoxia "AND" H^+ logic gate was contained to guarantee the tumor-specific gene mutation. Briefly, the generation of H^+ and O_2 consumption *via* GOx, and the limited O_2 generation by inhibiting CAT expression promoted the biodegradation of SALC. Meanwhile, the H_2O_2-mediated and starvation combinatorial multimodal antitumor effect was achieved *via* the resulting H_2O_2 and consumption of glucose from the GOx-catalyzed oxidation reaction, the accumulation of H_2O_2 from DNAzyme-mediated CAT silence where the ZIF-8-enhanced Zn^{2+} ions served as effective cofactors. All these regulations affected cellular homeostasis and amplified gene editing, which selectively killed tumor cells without unwanted genetic mutation in normal tissue. Collectively, this design highlights the great potential of biocomputing-based CRISPR delivery in complex physiological environments for precision medicine. Indeed, it is a slight step to *in vivo* biocomputing and site-specific gene editing but must inspire the development of general intelligent programmed

devices with the hierarchical organization for on-demand outputs after receiving particular signals in the future.

Acknowledgments

This work was financially supported by the National Natural Science Foundation of China (21874066, and 82073288), the National Key R&D Program of China (2019YFA0709200), the Key Research and Development Program of Jiangsu Province (BE2021373, China), Jiangsu Provincial Medical Key Discipline Cultivation Unit (JSDW202239, China), the Natural Science Foundation of Jiangsu Province (BK20200336, China), the Fundamental Research Funds for Central Universities (China), the Program for Innovative Talents and Entrepreneur in Jiangsu (China), and Postgraduate Research & Practice Innovation Program of Jiangsu Province (KYCX23_0146, China).

Author contributions

Yongchun Pan and Xiaowei Luan contributed equally to this work. Yujun Song and Bangshun He conceived the idea and designed the experiments. Yongchun Pan and Xiaowei Luan. Performed the majority of experimental work. Xuyuan Wang performed TEM characterization of materials. Fei Zeng, Shurong Qin, Qianglan Lu, Guanzhong He, and Yanfeng Gao performed the *in vivo* experiments. Yongchun Pan and Xiaowei Luan wrote the manuscript with feedback from all the authors. Yujun Song, Bangshun He, Xin Han and Xiaolian Sun supervised the project.

Conflicts of interest

The authors have no conflicts of interest to declare.

Appendix A. Supporting information

Supporting data to this article can be found online at https://doi.org/10.1016/j.apsb.2023.09.016.

References

1. Ivanov NM, Baltussen MG, Regueiro CLF, Derks MTGM, Huck WTS. Computing arithmetic functions using immobilised enzymatic reaction networks. *Angew Chem Int Ed* 2023;**62**:e202215759.
2. Wang Z, Yang J, Qin G, Zhao C, Ren J, Qu X. An intelligent nanomachine guided by DNAzyme logic system for precise chemodynamic therapy. *Angew Chem Int Ed* 2022;**61**:e202204291.
3. Pan Y, Qiu W, Li Q, Zhu S, Lin C, Zeng W, et al. Assembling two-phase enzymatic cascade pathways in pickering emulsion. *ChemCatChem* 2019;**11**:1878−83.
4. Chen M, Wang C, Ding Z, Wang H, Wang Y, Liu Z. A Molecular logic gate for developing "AND" logic probes and the application in hepatopathy differentiation. *ACS Central Sci* 2022;**8**:837−44.
5. de Bruin EC, McGranahan N, Mitter R, Salm M, Wedge DC, Yates L, et al. Spatial and temporal diversity in genomic instability processes defines lung cancer evolution. *Science* 2014;**346**:251−6.
6. Lee WC, Diao L, Wang J, Zhang J, Roarty EB, Varghese S, et al. Multiregion gene expression profiling reveals heterogeneity in molecular subtypes and immunotherapy response signatures in lung cancer. *Mod Pathol* 2018;**31**:947−55.
7. Pasha N, Turner NC. Understanding and overcoming tumor heterogeneity in metastatic breast cancer treatment. *Nat Can (Ott)* 2021;**2**:680−92.
8. Wang Y, Sun S, Zhang Z, Shi D. Nanomaterials for cancer precision medicine. *Adv Mater* 2018;**30**:1705660.
9. Badeau BA, Comerford MP, Arakawa CK, Shadish JA, DeForest CA. Engineered modular biomaterial logic gates for environmentally triggered therapeutic delivery. *Nat Chem* 2018;**10**:251−8.
10. Zhang P, Gao D, An K, Shen Q, Wang C, Zhang Y, et al. A programmable polymer library that enables the construction of stimuli-responsive nanocarriers containing logic gates. *Nat Chem* 2020;**12**:381−90.
11. Luo C, Sun J, Liu D, Sun B, Miao L, Musetti S, et al. Self-assembled redox dual-responsive prodrug-nanosystem formed by single thioether-bridged paclitaxel-fatty acid conjugate for cancer chemotherapy. *Nano Lett* 2016;**16**:5401−8.
12. Zhang H, Li Z, Gao C, Fan X, Pang Y, Li T, et al. Dual-responsive biohybrid neutrobots for active target delivery. *Sci Robot* 2021;**6**:eaaz9519.
13. Chen X, Soeriyadi AH, Lu X, Sagnella SM, Kavallaris M, Gooding JJ. Dual bioresponsive mesoporous silica nanocarrier as an "AND" logic gate for targeted drug delivery cancer cells. *Adv Funct Mater* 2014;**24**:6999−7006.
14. Yu F, Shang X, Zhu Y, Lou H, Liu Y, Meng T, et al. Self-preparation system using glucose oxidase-inspired nitroreductase amplification for cascade-responsive drug release and multidrug resistance reversion. *Biomaterials* 2021;**275**:120927.
15. Li X, Pan Y, Chen C, Gao Y, Liu X, Yang K, et al. Hypoxia-responsive gene editing to reduce tumor thermal tolerance for mild-photothermal therapy. *Angew Chem Int Ed* 2021;**60**:21200−4.
16. Luan X, Pan Y, Zhou Y, Zhou D, Zhao W, Zeng F, et al. Targeted self-assembly of renal clearable $Cu_{2-x}Se$ to induce lysosome swelling for multimodal imaging guided photothermal/chemodynamic synergistic Therapy. *Adv Funct Mater* 2022;**32**:2208354.
17. Fu LH, Wan Y, Qi C, He J, Li C, Yang C, et al. Nanocatalytic theranostics with glutathione depletion and enhanced reactive oxygen species generation for efficient cancer therapy. *Adv Mater* 2021;**33**:2006892.
18. Kiraga Ł, Cheda Ł, Taciak B, Różańska K, Tonecka K, Szulc A, et al. Changes in hypoxia level of CT26 tumors during various stages of development and comparing different methods of hypoxia determination. *PLoS One* 2018;**13**:e0206706.
19. Feng B, Hou B, Xu Z, Saeed M, Yu H, Li Y. Self-amplified drug delivery with light-inducible nanocargoes to enhance cancer immunotherapy. *Adv Mater* 2019;**31**:1902960.
20. Wu X, Yue H, Zhang Y, Gao X, Li X, Wang L, et al. Packaging and delivering enzymes by amorphous metal-organic frameworks. *Nat Commun* 2019;**10**:5165.
21. Li Y, Zhao P, Gong T, Wang H, Jiang X, Cheng H, et al. Redox dyshomeostasis strategy for hypoxic tumor therapy based on DNAzyme-loaded electrophilic ZIFs. *Angew Chem Int Ed* 2020;**59**:22537−43.
22. Xu Q, Pan Y, Liu X, Gao Y, Luan X, Zeng F, et al. Hypoxia-responsive platinum supernanoparticles for urinary microfluidic monitoring of tumors. *Angew Chem Int Ed* 2022;**61**:e202114239.
23. Geng W-C, Jia S, Zheng Z, Li Z, Ding D, Guo DS. A noncovalent fluorescence turn-on strategy for hypoxia imaging. *Angew Chem Int Ed* 2019;**58**:2377−81.
24. Tregubov AA, Nikitin PI, Nikitin MP. Advanced smart nanomaterials with integrated logic-gating and biocomputing: dawn of theranostic nanorobots. *Chem Rev* 2018;**118**:10294−348.
25. Gheghiani L, Wang L, Zhang Y, Moore XTR, Zhang J, Smith SC, et al. PLK1 induces chromosomal instability and overrides cell-cycle checkpoints to drive tumorigenesis. *Cancer Res* 2021;**81**:1293−307.
26. Jinek M, Chylinski K, Fonfara I, Hauer M, Doudna JA, Charpentier E. A programmable dual-RNA-guided DNA endonuclease in adaptive bacterial immunity. *Science* 2012;**337**:816−21.

27. Cong L, Ran FA, Cox D, Lin S, Barretto R, Habib N, et al. Multiplex genome engineering using CRISPR/Cas systems. *Science* 2013;**339**: 819−23.
28. Katti A, Diaz BJ, Caragine CM, Sanjana NE, Dow LE. CRISPR in cancer biology and therapy. *Nat Rev Cancer* 2022;**22**:259−79.
29. Wang HX, Li M, Lee CM, Chakraborty S, Kim HW, Bao G, et al. CRISPR/Cas9-based genome editing for disease modeling and therapy: challenges and opportunities for nonviral delivery. *Chem Rev* 2017;**117**:9874−906.
30. Li Z, Pan Y, Du S, Li Y, Chen C, Song H, et al. Tumor-microenvironment activated duplex genome-editing nanoprodrug for sensitized near-infrared titania phototherapy. *Acta Pharm Sin B* 2022;**12**: 4224−34.
31. Li L, Yang Z, Zhu S, He L, Fan W, Tang W, et al. A rationally designed semiconducting polymer brush for NIR-II imaging-guided light-triggered remote control of CRISPR/Cas9 genome editing. *Adv Mater* 2019;**31**:1901187.
32. Tang H, Xu X, Chen Y, Xin H, Wan T, Li B, et al. Reprogramming the tumor microenvironment through second-near-infrared-window photothermal genome editing of PD-L1 mediated by supramolecular gold nanorods for enhanced cancer immunotherapy. *Adv Mater* 2021; **33**:2006003.
33. Wang P, Zhang L, Zheng W, Cong L, Guo Z, Xie Y, et al. Thermo-triggered release of crispr-cas9 system by lipid-encapsulated gold nanoparticles for tumor therapy. *Angew Chem Int Ed* 2018;**57**: 1491−6.
34. Yang X, Tang Q, Jiang Y, Zhang M, Wang M, Mao L. Nanoscale ATP-responsive zeolitic imidazole framework-90 as a general platform for cytosolic protein delivery and genome editing. *J Am Chem Soc* 2019; **141**:3782−6.
35. Chen G, Abdeen AA, Wang Y, Shahi PK, Robertson S, Xie R, et al. A biodegradable nanocapsule delivers a Cas9 ribonucleoprotein complex for *in vivo* genome editing. *Nat Nanotechnol* 2019;**14**: 974−80.
36. Pu Y, Yin H, Dong C, Xiang H, Wu W, Zhou B, et al. Sono-controllable and ROS-sensitive CRISPR-Cas9 genome editing for augmented/synergistic ultrasound tumor nanotherapy. *Adv Mater* 2021;**33**:2104641.